Science of the Total Environment 778 (2021) 146266

Contents lists available at ScienceDirect

Science of the Total Environment

journal homepage: www.elsevier.com/locate/scitotenv

# Ferric iron incorporation promotes brushite hydrolysis and enhances cadmium immobilization

Jianan Guo [a,b,c], Xiaohang Zhang [a,b,c], Maolin Wang [a,b,c], Shijun Wu [a,b,*], Fanrong Chen [a,b], Yongqiang Yang [a,b]

[a] CAS Key Laboratory of Mineralogy and Metallogeny & Guangdong Provincial Key Laboratory of Mineral Physics and Materials, Guangzhou Institute of Geochemistry, Chinese Academy of Sciences, 511 Kehua Street, 510640 Guangzhou, China
[b] CAS Center for Excellence in Deep Earth Science, 511 Kehua Street, 510640 Guangzhou, China
[c] University of Chinese Academy of Sciences, 19 Yuquan Road, 100049 Beijing, China

## HIGHLIGHTS

- $Fe^{3+}$ incorporation decreased the interstitial water of DCPD.
- $Fe^{3+}$ incorporation accelerates the dehydration and hydrolysis rate of DCPD.
- The $Fe^{3+}$-bearing DCPD exhibited a higher Cd removal capacity and faster conversion kinetics to HA than the Fe-free DCPD.
- The DCPD-HA conversion significantly enhanced the stability of Cd in solid.

## GRAPHICAL ABSTRACT

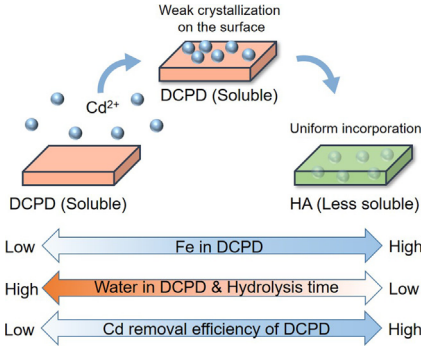


## ARTICLE INFO

*Article history:*
Received 2 November 2020
Received in revised form 27 February 2021
Accepted 28 February 2021
Available online 8 March 2021

Editor: Xinbin Feng

*Keywords:*
Brushite
Transformation
Hydrolysis
Incorporation
Cd immobilization

## ABSTRACT

Dissolution-precipitation processes on the surface of brushite (dicalcium phosphate dihydrate, DCPD) control the migration and transformation of potentially harmful elements (PHEs). The incorporation of impurities could affect the properties of DCPD and its interactions with PHEs. In this study, we synthesized $Fe^{3+}$-bearing DCPD via coprecipitation and investigated the influence of $Fe^{3+}$ incorporation on the crystal structure, hydrolysis process, and Cd removal performance. Fe-bearing DCPD had lattice expansion due to the coupled substitution of $Fe^{3+}$ and $NH_4^+$ for $Ca^{2+}$. Therefore, the Cd removal performance of Fe-DCPD was enhanced, with a maximum Cd uptake capacity of 431.6 mg/g, which is 1.77 times that of Fe-free DCPD (244.4 mg/g). Furthermore, Fe-DCPD also exhibited a faster hydrolysis rate, which was up to 2.67 times that of Fe-free DCPD and accelerated Cd's transfer to the stable host mineral, hydroxylapatite. Cd was first caught by the DCPD surface in a weakly crystalline form and then incorporated into the hydroxylapatite structure during crystallization. Based on the X-ray photoelectron spectroscopy and thermogravimetric analysis results, we concluded that the decrease in interstitial water due to Fe incorporation was responsible for accelerating hydrolysis and enhancing Cd immobilization. In all, the incorporation of $Fe^{3+}$ into DCPD could promote its transformation and improve its Cd uptake capacity. Our results suggest that Fe-DCPD could be a promising candidate for environmental remediation.



## 1. Introduction

Cd is one of the most dangerous potentially harmful elements (PHEs) and poses a threat to human health. For example, it can cause damage to kidneys, bones, and the neural system, and has significant

* Corresponding author at: CAS Key Laboratory of Mineralogy and Metallogeny & Guangdong Provincial Key Laboratory of Mineral Physics and Materials, Guangzhou Institute of Geochemistry, Chinese Academy of Sciences, 511 Kehua Street, 510640 Guangzhou, China.
*E-mail address:* wus@gig.ac.cn (S. Wu).

https://doi.org/10.1016/j.scitotenv.2021.146266
0048-9697/

carcinogenicity (Järup and Åkesson, 2009; Waalkes, 2000). Owing to its extreme toxicity, the International Agency for Research on Cancer (IARC) has classified Cd and Cd compounds as Class 1 human carcinogens (IARC, 1993), and the maximum acceptable Cd concentration in drinking water is 3 μg/L, according to the World Health Organization (WHO) (WHO, 2011). On the other hand, the binding capacity of Cd in the soil is weaker than other PHEs, which makes it susceptible to mobilization and migration (Tang et al., 2011). Adsorption, precipitation, and isomorphic replacement at the mineral-water interface are effective and inexpensive methods of lowering the chemical reactivity and mobility of PHEs in soil and water (Alexandratos et al., 2007; Song et al., 2020; Yukselen and Alpaslan, 2001). Among the numerous available adsorbents/immobilizers, calcium phosphate minerals (CaPs) have attracted widespread attention as they are non-toxic and inexpensive. Hydroxylapatite (HA, $Ksp = 10^{-116.8}$) (Wang and Nancollas, 2008), the most stable CaP under neutral to alkaline conditions, is considered to be ideal storage for Cd remediation (Conca and Wright, 2006; Knox et al., 2003).

Brushite, i.e., $CaHPO_4{\cdot}2H_2O$ (dicalcium phosphate dihydrate, DCPD, $Ksp = 10^{-6.59}$), is the most soluble crystalline precursor mineral of HA, and has been used as a phosphate fertilizer for decades (Bouldin and Sample, 1959; Mansour et al., 2016). Also, DCPD precipitates as a reaction product during the agricultural application of other phosphorus fertilizers, such as monocalcium phosphate (MCP) (Chien et al., 2011) and livestock manure (Kar et al., 2017). DCPD is thermodynamically unstable under pH values greater than 6.5 and can transform into stable HA by hydrolysis (Rubini et al., 2019; Tas, 2016; Ucar et al., 2017). DCPD-containing CaP is more active than HA in the immobilization of lead (Pb), where it forms Pb-apatite at the external surface (Pham Minh et al., 2014). Moreover, DCPD immobilizes Cd more efficiently than HA as it can provide more $PO_4^{3-}$ during transformation (Zhai et al., 2018).

Ion impurities can be incorporated into the structure of DCPD, affecting its physicochemical properties and microstructure (Liu et al., 2015; Schumacher and Gelinsky, 2015). Such variations are expected to influence the surface reactivity of DCPD and its interactions with PHEs. For example, the substitution of potassium in DCPD accelerates its transformation (Kumar et al., 1999), while magnesium incorporation prevents its conversion by inhibiting the dissolution of DCPD (Lee and Kumta, 2010). Fe is one of the most abundant elements in the Earth's crust (Chaturvedi and Dave, 2012; Colombo et al., 2014; Frey and Reed, 2012), and plays a crucial role in the geochemical cycle of various PHEs (Cundy et al., 2008). Fe is also a relatively abundant element in many cultivated soils, with average total concentrations of 20 to 40 g/kg (Colombo et al., 2014). As a redox-sensitive element, the most abundant Fe oxidation states in natural environments are reduced ferrous Fe ($Fe^{2+}$) and oxidized ferric Fe ($Fe^{3+}$) (Crichton et al., 2001; Melton et al., 2014). However, the effect of Fe incorporation on the DCPD hydrolysis process and its PHEs immobilization capacity is poorly understood.

Therefore, we prepared $Fe^{3+}$-bearing DCPD by coprecipitation and investigated the influence of Fe on its crystal structure, morphology, and thermal stability. The hydrolysis kinetics of the synthesized DCPD and its Cd removal capacity were subsequently investigated. To our best knowledge, this is the first investigation into the effect of incorporated trivalent metal on the transformation of DCPD. The results of this study will further our understanding of the transformation process of impurity-bearing phosphate minerals in the natural environment and aid in developing promising environmental remediation materials.

## 2. Methodology

### 2.1. DCPD synthesis

Fe-free and Fe-bearing DCPD were synthesized via coprecipitation according to the following reaction: $xFe^{3+} + (1-x)Ca^{2+} + HPO_4^{2-} = Ca_{(1-x)}Fe_xHPO_4 \cdot 2H_2O$. In brief, a mixed solution containing 0.3 mol/L of $Fe^{3+}$ and $Ca^{2+}$ chloride salts (Solution A) with a molar ratio of $x/(1-x)$ was prepared first ($x = 0$, 2%, 5%, and 10%). Then, 100 mL of solution A was added to 100 mL of solution B, which contained 0.3 mol/L $(NH_4)_2HPO_4$, dropwise using a peristaltic pump (flow rate: 2 mL/min), under continuous stirring (400 r/min) at room temperature (RT, ~25 °C) for 1 h. After 48 h, the suspension was vacuum-filtrated, washed several times using deionized water, and then freeze-dried for 24 h. All precipitates were then stored in a drying environment for further characterization and experiments and labeled as Fe0, Fe2, Fe5, and Fe10 according to the Fe/(Fe + Ca) molar ratio used for synthesis.

### 2.2. DCPD hydrolysis kinetics

The DCPD hydrolysis was conducted in a 0.05-M Tris-HCl solution with an initial pH of 8.2, which was adjusted using 0.01-M HCl. Approximately 0.50 g of DCPD was loaded into a 200-mL corked flask, resuspended in 100 mL of Tris-HCl solution, and homogenized using an RT magnetic stirrer. During hydrolysis, 5-ml of the suspension was sampled and the solution pH was monitored at regular time intervals until it remained stable. Samples were denoted as X-t, where X represents the initial sample name, and t represents the hydrolysis time (min).

### 2.3. Immobilization of Cd

Owing to the remarkable inhibition of DCPD hydrolysis by Cd (Fig. S1), the DCPD was transformed in a Cd-containing solution at 40 °C by mixing 100 mg of DPCD with 20 mL of a 0.05-M Tris-HCl solution containing Cd in a 50-mL centrifugal tube. The Cd concentration ranged from 0.1 to 30 mM in different tubes, which were capped and shaken using an overhead shaker in an incubator chamber for 14 d to ensure complete DCPD hydrolysis. The suspension was then centrifuged and filtered using a 22-μm filter membrane. The supernatant was used for chemical analysis, while the precipitates were freeze-dried and stored for further characterization. Individual kinetics studies of Cd immobilization were conducted during the hydrolysis of DCPD using a 5-mM Cd solution under similar conditions. After sampling, the reaction solution was immediately centrifuged and filtered through a 22-μm filter membrane. The precipitates were denoted as X-y-t, where X represents the initial sample name, y represents the Cd concentration in the initial solution (mM), and t represents the hydrolysis time (h).

### 2.4. Stability of Cd in DCPD and HA

Dissolution experiments were conducted to study the long-term stability of Cd using DCPD hydrolyzed in a 0.05-mM Cd solution after 12 and 24 h, i.e., DCPD-5-12 and DCPD-5-24. The Cd content of each sample used for the dissolution experiments is provided in Table S1. Briefly, 0.10 g of the solid was transferred into a 15-mL polypropylene centrifuge tube filled with 10 mL of distilled water with pH values of 2.0, 7.0, and 10.0. The tubes were capped and shaken using an overhead shaker (40 rpm) in an RT incubator chamber. After seven days, all of the samples were centrifuged and filtered to conduct the filtrate's chemical analysis.

### 2.5. Characterization

#### 2.5.1. Powder X-ray diffraction

Powder X-ray diffraction (XRD) was conducted to identify the mineral phases and transformation products of the synthesized samples. The XRD patterns were obtained using a Bruker D8 Advance diffractometer (Bruker AXS, Germany) with a Ni filter and Cu Kα radiation ($\lambda = 0.154$ nm) at 40 kV and 40 mA. All patterns were recorded between 3° and 80° (2θ) at a scan rate of 3.0° (2θ) per minute. The unit cell parameters of the DCPD were calculated using Jade 6.5. Meanwhile, temperature-dependent XRD studies were conducted to investigate the thermal stability of DCPD using the same X-ray diffractometer equipped with a heating stage from RT to 180 °C at a heating rate of

5 °C/min. The temperature-dependent XRD patterns were collected at RT, 100, 120, 140, 160, and 180 °C, with an interval of 10°/min between 10° and 70° (2θ). The products obtained at different temperatures were denoted as X-T, where X represents the initial sample name, and T represents the temperature (°C). For example, Fe0_100 °C represents Fe0 after heating at 100 °C.

*2.5.2. Thermogravimetric analysis*

A Netzsch STA 409PC instrument was used to conduct thermogravimetric analysis (TGA). Briefly, approximately 15 mg of DCPD was heated from RT to 300 °C at a heating rate of 5 °C/min in a corundum crucible under a pure $N_2$ atmosphere (60 mL/min). The differential thermogravimetric (DTG) curves were then derived from the TG data.

*2.5.3. Fourier-transform infrared spectroscopy*

The Fourier-transform infrared (FTIR) spectral measurements were obtained using a Brucker Vertex-70 following the KBr method (0.90 mg of sample powders and 80.00 mg of KBr) at RT in the range of 4000–400 $cm^{-1}$ with a resolution of 4 $cm^{-1}$ and scan number of 64.

*2.5.4. X-ray photoelectron spectroscopy*

The surface element information of selected samples was obtained by X-ray photoelectron spectroscopy (XPS) using a Thermo Fisher K-Alpha instrument equipped with an Al Kα source. The pass energies of wide and narrow scanning were set to 100 and 30 eV, respectively, and the binding energies of all peaks were calibrated using the C1s standard spectrum (284.8 eV). The depth of XPS analysis is approximately 6 nm (Viipsi et al., 2013). The elemental atomic ratio was analyzed based on the integration of the XPS peaks using Thermo Scientific Avantage software.

*2.5.5. Morphology observation*

A field emission scanning electron microscope (SEM; SU8010, 1.5 kV) and transmission electron microscope (TEM; FEI Talos F200s, 200 kV) were used to observe the morphology of the precipitates. Meanwhile, the attached energy-dispersive X-ray spectroscope (EDS, FEI Super-X EDS) was used to determine the samples' chemical composition.

*2.5.6. Chemical analysis and pH measurement*

The Ca, Fe, P, and Cd concentrations in the filtrate solution were analyzed using an inductively coupled plasma-optical emission spectrometer (ICP-OES, VARIAN VISTA PRO), and the solution pH was measured using a pre-calibrated pH meter (Sartorius, PB-10). ICP-OES analyzed the selected solids' elemental content after digestion (20 mg solid in 1 mL of concentrated $HNO_3$) and dilution.

*2.6. Data processing*

The amount of removed Cd (q, mg/g) and Cd removal efficiency ($R_d$, %) by DCPD was calculated using Eqs. (1) and (2), respectively.

$$q = (C_0 - C_t) \times V/m \tag{1}$$

$$R_d = \frac{C_t}{C_0} \times 100\% \tag{2}$$

where $C_0$ (mg/L) is the initial Cd concentration, $C_t$ (mg/L) is the residual Cd concentration at time *t*, V (mL) is the volume of the solution, and m (mg) is the quality of DCPD.

The Cd release fraction (F, ‰) was calculated using Eq. (3).

$$F = \frac{C_p \times V_p}{Q_p \times m} \times 1000‰ \tag{3}$$

where $C_p$ (mg/L) is the released Cd concentration, $V_p$ (mL) is the volume of distilled water, $Q_p$ (mg/g) is the Cd content of each sample, and m (mg) is the mass of DCPD. The obtained data were processed using Microsoft Excel. All reported errors for the solution analysis represent the standard deviation of two replicate experiments.

## 3. Results and discussion

*3.1. XRD, FTIR, and SEM characterization of DCPD*

The XRD patterns of Fe-free (Fe0) and Fe-bearing DCPD (Fe2, Fe5, and Fe10) are shown in Fig. 1a. The patterns of all synthesized products corresponded well to that of the standard DCPD, and did not contain any peaks associated with iron oxides. Therefore, the ferric ions were successfully incorporated into DCPD instead of precipitating as iron oxide on its surface. The most intense diffraction of (020) at 11.7° for Fe-DCPD shifted left from that of Fe0 as the Fe loading increased, indicating the crystal lattice distortion and more significant interplanar spacings. Furthermore, the chemical analysis showed that the Ca content decreased with increasing Fe content, indicating Fe substitution for Ca (Table S2).

Theoretically, eight-coordinated $Fe^{3+}$ possesses a crystal radius of 0.92 Å, which is much lower than that of $Ca^{2+}$ with the same coordination (1.26 Å) (Shannon, 1976). Therefore, partial one-to-one replacement would result in smaller lattice parameters (Kim et al., 2003). However, the lattice's chemical expansion along the *b*- and *c*-axes was observed for the Fe-DCPD (Table S3). As it was necessary to maintain the charge balance, we proposed two possible explanations for such variations. (1) The substitution of $Fe^{3+}$ generated some lattice vacancies, resulting in a change in the chemical composition and structural distortion (Eq. (4)). (2) The coupled substitution of $Fe^{3+}$ and monovalent ions, i.e., $NH_4^+$, for two $Ca^{2+}$ sites (Eq. (5)) (Gupta et al., 2010; Shi et al., 2016). The crystal radius of nitrogen is 1.32 Å in $NH_4^+$ (Shannon, 1976), which contributed to the expansion of the lattice structure.

$$2Fe^{3+} + \square \leftrightarrow 3Ca^{2+} \tag{4}$$

$$Fe^{3+} + NH_4^+ \leftrightarrow 2Ca^{2+} \tag{5}$$

Fig. 1b shows the FTIR spectra of Fe0 and Fe-DCPD. The bands at 3544, 3478, 3266, and 3160 $cm^{-1}$ were assigned to the O—H stretching of water, and 1653 $cm^{-1}$ indicated the occurrence of residual free water. Meanwhile, P—O stretching (ν3) was observed at 1124, 1056, and 983 $cm^{-1}$, while P–O(H) stretching was observed at 874 $cm^{-1}$, and $H_2O$ liberation was recorded at 792 $cm^{-1}$. Finally, O-P-O(H) bending was observed at 660, 577, and 526 $cm^{-1}$. These IR band positions were generally consistent with previous studies (Bamzai et al., 2012; Mandel and Tas, 2010; Tas and Bhaduri, 2004). A new peak was observed at 1402 $cm^{-1}$ for Fe5 and Fe10, and its intensity increased with the iron content of DCPD. This peak belonged to the N—H deformation vibration peak for $NH_4^+$ (Gautier et al., 2010) and supported the coupled substitution of $Fe^{3+}$ and $NH_4^+$ for $Ca^{2+}$ (Eq. (5)).

Fig. 1c shows the SEM photomicrographs of the Fe0 and Fe-DCPD crystals. Fe0 exhibited a plate-like appearance with sharp edges and preferred to grow along the (010) crystalline plane, similar to previous studies (Sekar et al., 2009; Temizel et al., 2011). With the incorporation of $Fe^{3+}$, Fe-DCPD maintained the plate-like morphology, although more defects, sharp edges, and small crystals present. Additionally, the Fe-DCPD preferred to link with one another to form petal-like aggregates.

*3.2. Thermal stability of DCPD*

The XRD patterns in Fig. S2 show the mineral phase transformation of DCPD during heating. DCPD decomposed in the temperature range of 100 to 160 °C. As the temperature increased, the peak intensity at 11.7° (2θ) assigned to the (020) plane of DCPD gradually declined. Meanwhile, a new reflection appeared at 26.7° (2θ), indicating the generation of anhydrous monetite ($CaHPO_4$, dicalcium phosphate

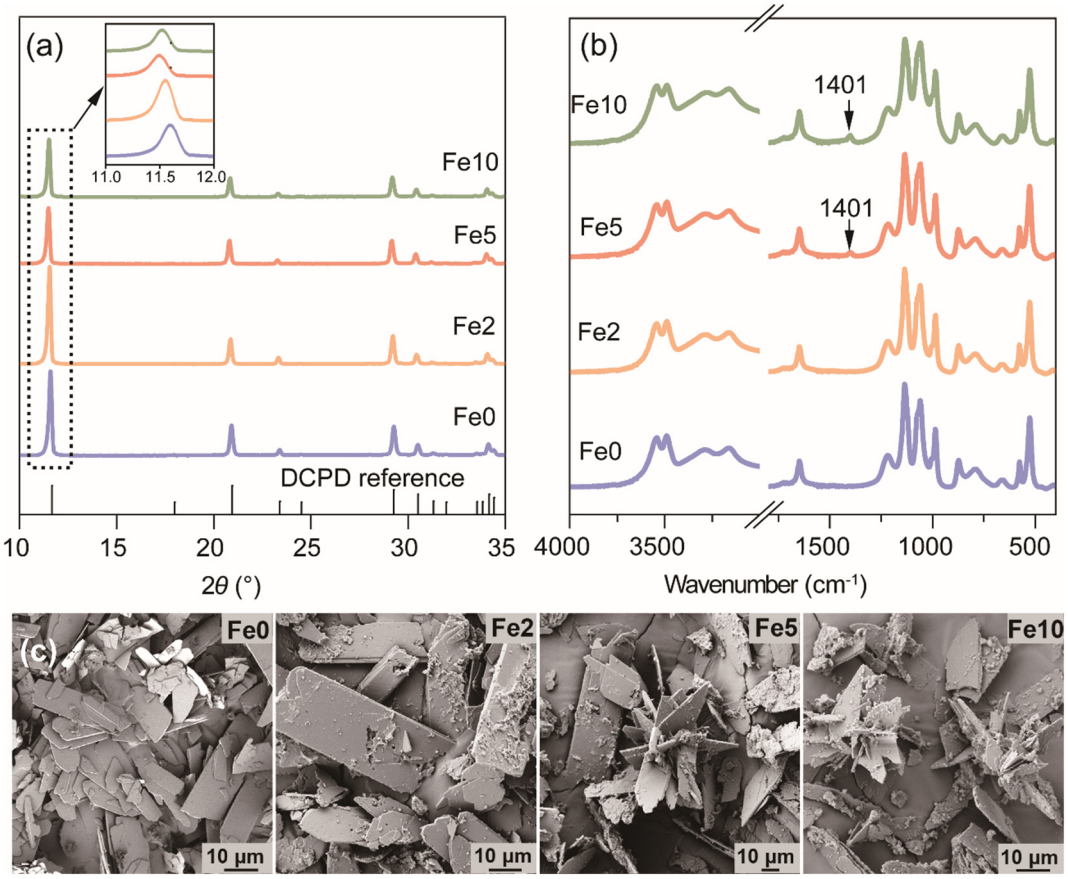


**Fig. 1.** XRD patterns (a), FTIR spectra (b), and SEM images (c) of DCPD (DCPD reference was obtained from the ICDD database with code number 01-072-0713).

anhydrous/DCPA). Upon heat treatment, all DCPD was converted into DCPA, which agreed with previous results (Dosen and Giese, 2011; Schofield et al., 2004). Fig. S3a presents the XRD patterns of DCPD after heating at 160 °C. Trace DCPD was present in Fe0_160 °C and Fe2_160 °C, as indicated by the characteristic peak at 11.7° (2θ). However, this peak was absent in Fe5_160 °C and Fe10_160 °C, suggesting that the decomposition of Fe5 and Fe10 was completed before 160 °C. This phenomenon demonstrates that the incorporation of $Fe^{3+}$ resulted in a lower Fe-DCPD collapse temperature than the Fe-free phase.

The TG curves of Fe0 and Fe-DCPD are shown in Fig. S3b, and illustrate that the thermal decomposition of DCPD into DCPA consisted of two water loss stages. The first stage of DCPD decomposition occurred at 130–140 °C, and the second decomposition stage occurred at 180–200 °C. Meanwhile, the DTG curves (Fig. S3c) of Fe0 and Fe-DCPD exhibited a leftward shift with increasing Fe content, suggesting that iron incorporation led to a deterioration in the thermal stability of DCPD, which agrees well with the XRD data. The total weight loss of Fe0 during heat treatment was 21.88%, which was close to the theoretical value according to Eq. 6. Notably, the weight loss during the thermal decomposition of Fe-DCPD was 21.55%, 20.65%, and 20.73%, respectively, which were slightly lower than Fe0 (Fig. S3b).

$$CaHPO_4{\cdot}2H_2O \rightarrow CaHPO_4 + 2H_2O \quad (6)$$

### 3.3. DCPD hydrolysis

DCPD transforms into octacalcium phosphate (OCP) or HA in aqueous solutions via hydrolysis based on different conditions (Madsen, 2008; Shih et al., 2004). Fig. 2a shows the XRD patterns of Fe0 and Fe-DCPD after hydrolysis in the Tris-HCl solution for 8 h. The characteristic diffraction peak of DCPD (2θ = 11.7°) completely disappeared, and only the distinct diffraction peaks of HA were observed. These results indicated that the incorporation of $Fe^{3+}$ did not change the DCPD hydrolysis products. The reaction equation for the hydrolysis of DCPD to HA in solution is provided in Eq. 7. The solution pH declined with the depletion of $OH^-$, which could be used as a marker for conversion (Madsen, 2008; Štulajterová and Medvecký, 2008; Ucar et al., 2017). As shown in Fig. 2b, the evolution of the solution pH during hydrolysis contained three stages. During Stage I, the pH declined slowly as the DCPD's surface dissolved. During Stage II, the pH declined rapidly when the system was supersaturated with HA, which nucleated on the crystal's surface. During Stage III, the pH slowly reached equilibrium. Theoretically, DCPD co-existed with HA in Stage II, while DCPD was present on Stage I and HA was only present at Stage III. Therefore, the hydrolysis of Fe0 to HA was completed within 360 min at RT. Comparably, the hydrolysis completion times for Fe2, Fe5, and Fe10 were 330, 320, and 240 min, respectively. These results suggest that the incorporated $Fe^{3+}$ accelerated the hydrolysis of DCPD.

$$10CaHPO_4{\cdot}2H_2O + 8OH^- \rightarrow Ca_{10}(PO_4)_6(OH)_2 + 4HPO_4^{2-} + 26H_2O \quad (7)$$

### 3.4. Immobilization of Cd

#### 3.4.1. Cd removal capacity

Fig. 3 shows the Cd uptake amounts and removal efficiency curves of the DCPD in solutions with different initial Cd concentrations. At initial Cd concentrations of 0.1–10 mM, the Cd uptake amounts exhibited a linear, positive relationship with the initial Cd concentrations, and the Cd removal efficiencies exceeded 95%. Subsequently, as the initial Cd concentration increased, the Cd uptake increased slowly and eventually reached equilibrium at an initial concentration of 30 mM. The maximum Cd uptake amounts of Fe2, Fe5, and Fe10 were 284.0, 353.1, and

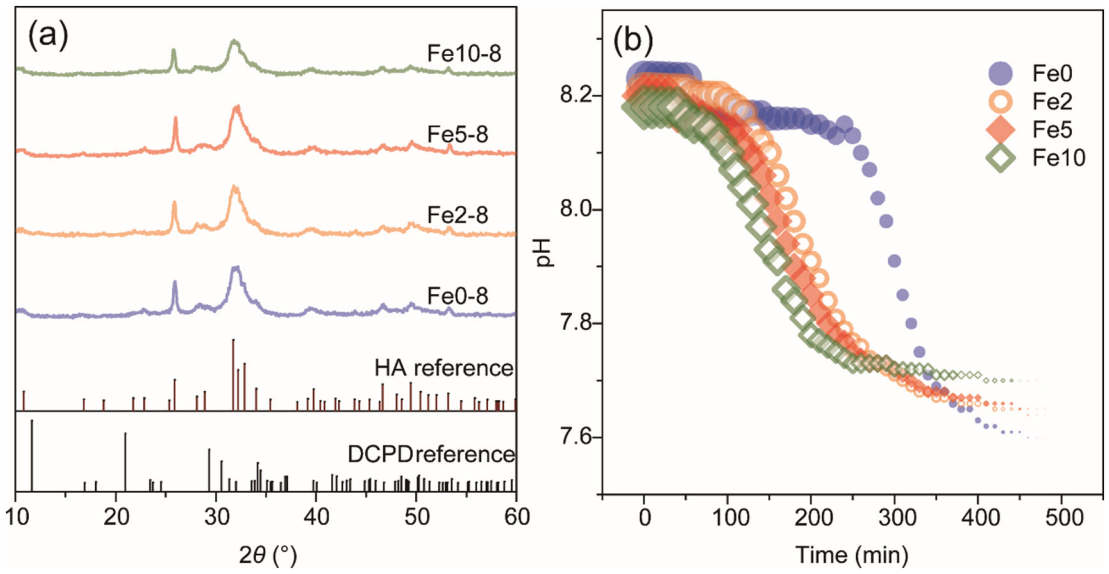


**Fig. 2.** XRD patterns of DCPD after hydrolysis for 8 h (a; DCPD and HA references were obtained from the ICDD database with code numbers 01-072-0713 and 01-089-6437) and evolution of the solution pH during the hydrolysis of DCPD (b).

431.6 mg/g, respectively, which were significantly higher than that of Fe0 (244.4 mg/g). That is, the Cd uptake by Fe-DCPD was 1.16–1.77 times that of Fe0, with Cd concentrations ranging from 20 to 30 mM. Fe-bearing DCPD exhibited an equal or higher removal capacity to other materials (Table 1), suggesting that it could be a promising material for the effective removal and immobilization of Cd.

*3.4.2. Cd removal kinetics*

A detailed kinetic study was conducted to further examine the removal of aqueous Cd by DCPD during conversion. As shown in Fig. 4a, the hydrolysis of DCPD in the Cd solution followed a similar pH evolution trend to that of the Cd-free solution. The hydrolysis of DCPD was remarkably inhibited in the Cd-containing solution, i.e., Stage II completed at 16, 10, 6, and 6 h for Fe0, Fe2, Fe5, and Fe10, respectively. The times required to reach equilibrium were 10.67, 6.67, 4.00, and 4.00 times that in the Cd-free solution (1.5 h, Fig. S1). It has been demonstrated that Cd strongly inhibits the nucleation of HA (Madsen et al., 2004), therefore, resulting in the extended conversion time of DCPD to HA in Cd-containing solutions.

The evolution of the aqueous Cd, Ca, and P concentrations during DCPD hydrolysis is shown in Fig. 4b–d. After 1 h of interaction, the Cd concentrations decreased from 562 to 61.97 (Fe0), 16.80 (Fe2), 11.66 (Fe5), and 9.86 mg/L (Fe10), with corresponding Cd removal efficiencies of 89.0%, 97.0%, 97.9%, and 98.2%, respectively. As mentioned previously, the mineral phase has not been changed at this time; the drastic decreases in the Cd concentration were attributed to adsorption or precipitation by DCPD. Meanwhile, Ca was released into the solution, with the concentration reaching 97.18 mg/L. The molar ratios of adsorbed Cd to released Ca ranged from 5.15 to 6.15, suggesting the partial exchange between Ca and Cd on the surface of the DCPD. Thereafter, the evolution of aqueous Ca followed the same trend as the solution pH.

The trends of aqueous P were opposite to the directions of the pH and Ca. Specifically, the concentration of aqueous P increased slowly at Stage I for 4 to 14 h, increased rapidly within the next 1 to 2 h

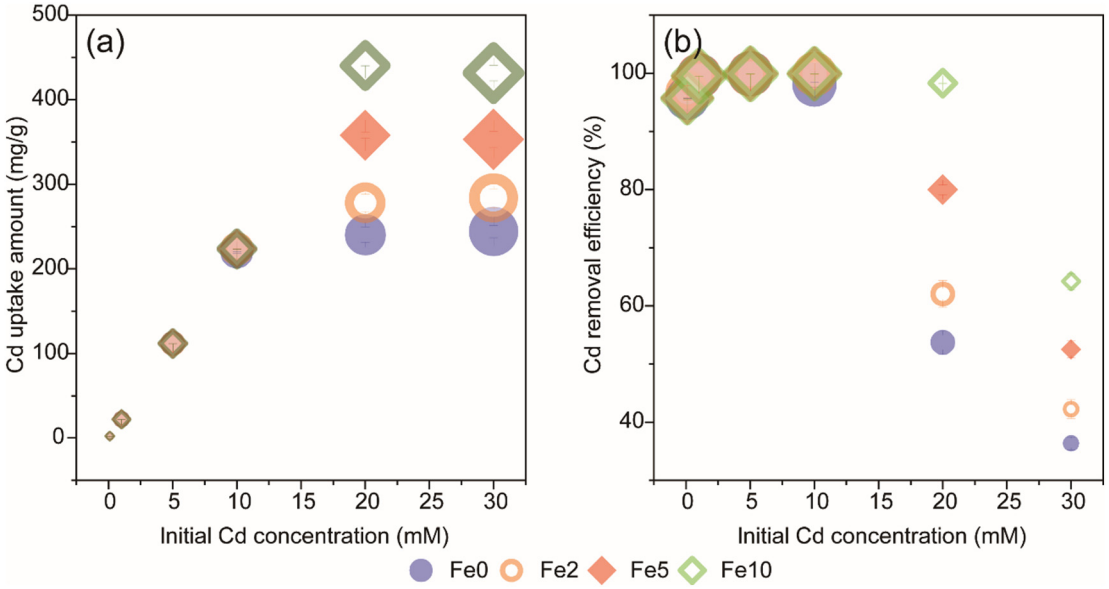


**Fig. 3.** Cd uptake amount (a) and removal efficiency (b) of DCPD at different initial Cd concentrations.

**Table 1**
Comparison of Cd-uptake capabilities by different materials.

| Material | Experimental method | Maximum uptake capacity (mg/g) | Initial pH | Temperature (°C) | Solid-liquid ratio (g/L) | Reference |
|---|---|---|---|---|---|---|
| Natural HA | Adsorption | 17.8 | 5.0 | RT | 2.0 | (Fernane et al., 2008) |
| Synthetic HA | Adsorption | 25.9 | 5.0 | RT | 2.0 | (Fernane et al., 2008) |
| Synthetic nano-HA | Adsorption | 88.5 | 7.0 | 25.0 | 10.0 | (Elkady et al., 2011) |
| Ca-deficient HA | Adsorption | 23.0 | 5.0–6.0 | RT | 0.8 | (Zhu et al., 2010) |
| $Fe_3O_4$/PANI/$MnO_2$ hybrids | Adsorption | 154.0 | 6.0 | RT | 1.0 | (Zhang et al., 2017) |
| Nanostructured $TiO_2$ | Adsorption | 396.0 | 5.0–6.0 | RT | / | (Zha et al., 2014) |
| Amorphous $MoS_3$ nanosheets | Adsorption | 383.1 | 6.0 | RT | 0.25 | (Fu et al., 2019) |
| Bone-biochar composites | Adsorption | 163.4 | 5.0 | 25.0 | 10.0 | (Xiao et al., 2020) |
| Magnetic graphene oxide | Adsorption | 128.2 | 5.0 | 25.0 | 1.0 | (Bao et al., 2020) |
| Biochar-supported hydrated manganese oxide | Adsorption | 156.0 | 5.0 | 25.0 | 0.2 | (Wan et al., 2018) |
| HA converted from calcite | Conversion | 369.2 | >9.0 | 70.0 | 2.0 | (Wang et al., 2019) |
| HA converted from Fe-free DCPD | Conversion | 244.4 | 8.0 | 40.0 | 5.0 | This study |
| Fe-HA converted from Fe-bearing DCPD | Conversion | 284.0–431.6 | 8.0 | 40.0 | 5.0 | This study |

(Stage II), and then remained stable in Stage III. The XRD results demonstrated that most of the DCPD was converted into HA at the end of Stage II (Fig. S4). Therefore, the formation of HA could be tracked by the rapid decreases in the solution pH and Ca concentration. Meanwhile, the remarkable increase in the P concentration also indicated HA formation. These data demonstrated that most of the aqueous Cd was first caught by DCPD and then immobilized by the newly formed HA with the other residual Cd in the solution. Furthermore, the solution's Fe concentration was always below the instrument's detection limit, suggesting that the HA immobilized almost all of the Fe in the DCPD.

### 3.5. Evolution of morphology

Fig. S5a provides the SEM images of Fe0 after immersion in the Cd-free Tris-HCl solution for 2 h. According to the solution pH, the dominant phase of the solid was DCPD. Some of the DCPD retained its plate-like morphology (Area A), while other crystals were converted, with nanoplate phases growing on the surface (Area B). These new precipitates were composed of nanosheets in a mesh-like structure, which were significantly different to the typical hexagonal columnar morphology of HA (Rakovan, 2002) and close to that of Ca-deficient hydroxyapatite (CDHA, Ca/$P = 1.5$) (Camiré et al., 2005). As confirmed previously, CDHA could be the conversion product of DCPD in an aqueous solution (Tas and Bhaduri, 2004). The morphology of the Fe10 transformation products was the same as that of Fe0 (Fig. S5b).

When Fe10 was transformed in the 5-mM Cd solution for 2 h, the bulk material retained its original plate morphology (Fig. 5a). Notably, new nanoparticles formed irregular nanowires on the surface. The elemental mapping results showed that the nanowires enriched in the distribution of Cd were inversely related to the distribution of Ca (Fig. 5d and e). The selected area electron diffraction (SAED) results indicated that these new nanoparticles were weakly crystalline (Fig. 5f). Madsen et al. (2004) reported that Cd could inhibit the HA nucleation process by forming Cd-bearing amorphous calcium phosphate. Therefore, it is likely that the weakly crystalline Cd-rich nanowires in our experiment hindered the transformation of DCPD by inhibiting the nucleation of HA. After completing the conversion, mesh-like nanosheets similar to those in the Cd-free solution were observed (Fig. 5b). The high-resolution transmission electron microscopy (HRTEM) and fast Fourier-transform (FFT) diffraction pattern (Fig. 5h) show the d-spacing (0.281 nm) of the lattice planes related to the (211) reflection of HA, further confirming the crystalline structure following transformation. EDS analysis (Fig. 5i) confirmed that Cd and Fe were incorporated in the transformed apatite.

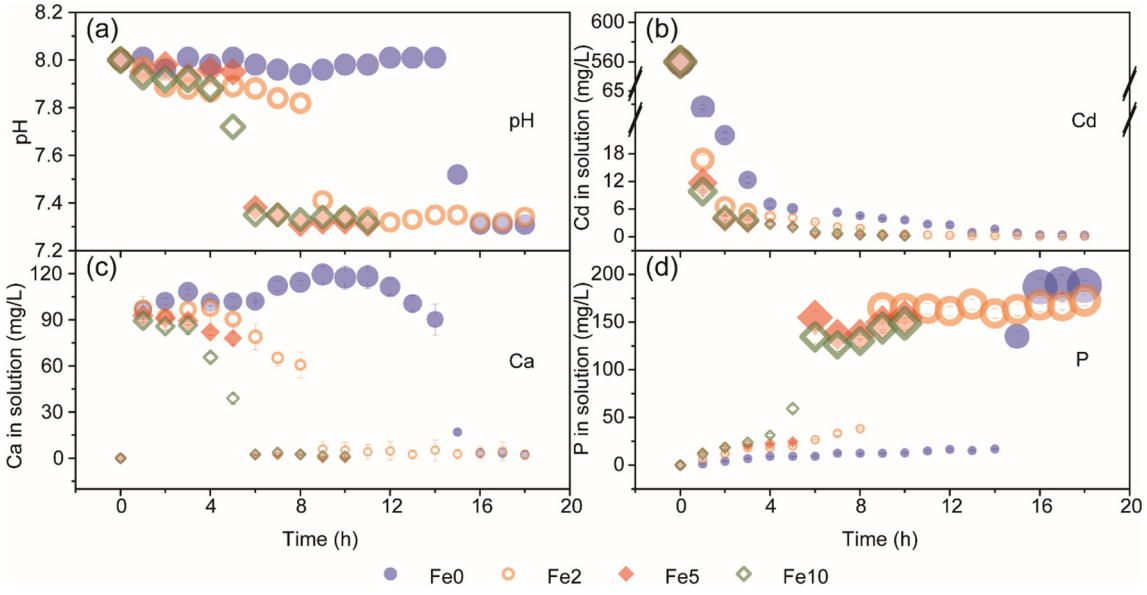


**Fig. 4.** Evolution of the aqueous pH (a) and Cd (b), Ca (c), and P (d) concentrations during the hydrolysis of DCPD in the Tris-HCl solution containing 5 mM of Cd.

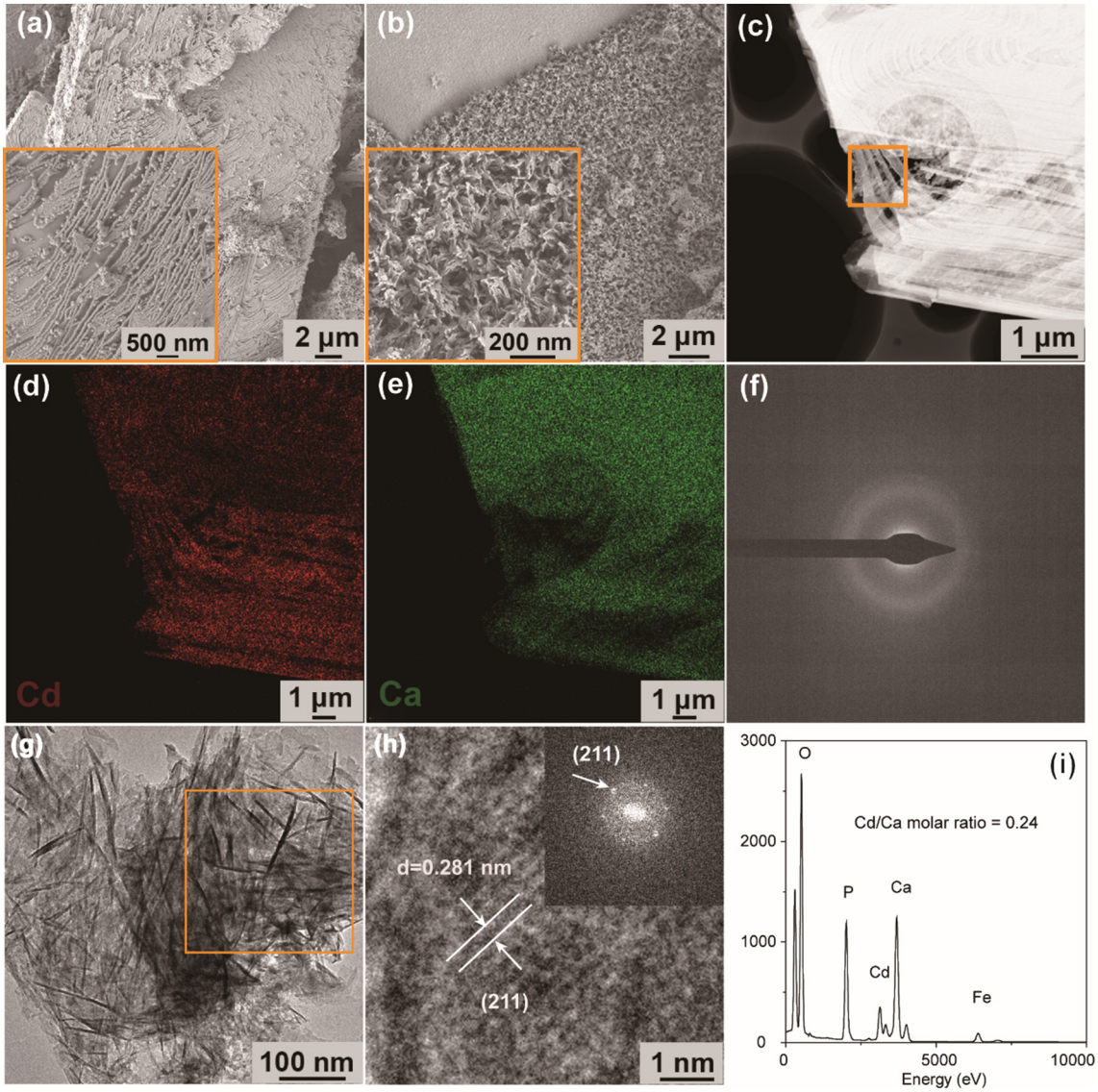


**Fig. 5.** SEM images of Fe10-5-2 (a) and Fe10-5-8 (b). TEM image (c), correlated TEM-EDS elemental mapping (d, e), and SAED (f) of Fe10-5-2. TEM image (g), HRTEM and FFT image (h), and EDS spectrum (i) of Fe10-5-8.

### 3.6. Release of Cd

Fig. 6 shows the release of Cd during the dissolution of DCPD and its hydrolysis products. After dissolution for seven days in the solution with an initial pH of 3.0, Fe0-5-12 released 1.63‰ Cd, while Fe0-5-24 released 0.14‰ Cd, with a remarkable decline of 91.4%. The amount of Cd released from all Fe-DCPD samples was below 0.11‰, regardless of the solution pH and hydrolysis time. As stated above, the mineral phase of Fe0-5-12 was DCPD, while Fe0-5-24 and all Fe-DCPD samples used in the dissolution experiments were HA. Our data demonstrated that Cd immobilized by HA was less soluble than Cd adsorbed by DCPD, as expected. Furthermore, the amount of Cd released by all samples was negatively correlated with the initial solution pH. At the same initial pH, the amount of Cd released from HA was negatively related to the solid Fe content (Fig. 6b).

### 3.7. DCPD transformation and Cd removal mechanisms

Generally, DCPD-HA transformation begins as the surface dissolution of DCPD, followed by the nucleation and growth of HA (Štulajterová and Medvecký, 2008). The dissolution of DCPD provides $Ca^{2+}$ and $PO_4^{3-}$, which are necessary for HA nucleation. When Cd is present, its migration and distribution are associated with the transformation of DCPD-HA. To further elucidate the Cd removal mechanism, the surface and bulk elemental composition of the transformation products of Fe10 were determined by XPS and complete dissolution, respectively. Fig. 7a shows the evolution of the surface and bulk Cd/Ca molar ratio of the solid phase during the transformation of DCPD to HA. After 1 h of interaction, the Cd/Ca molar ratio on the surface was 1.04, which was 4.95 times the bulk Cd/Ca molar ratio (0.21). Combining these findings with the SEM and TEM results, the removal of Cd in the early stage was attributed to the precipitation of weakly crystalline Cd-rich nanowires on the surface of DCPD. The Cd/Ca molar ratio on the surface of the sample began to decrease significantly from the third to the sixth hour and gradually approached the bulk Cd/Ca molar ratio, suggesting that the Cd in the solid phase was converted from surface enrichment to homogeneous distribution. The mineral phase evolution (Fig. S4) and change in the aqueous P concentration (Fig. 7b) indicated that HA nucleated and grew during this period (3–6 h).

Viipsi et al. (2013) investigated crystalline HA interaction with $Cd^{2+}$ and founded that Cd was enriched on the surface as a solid-solution

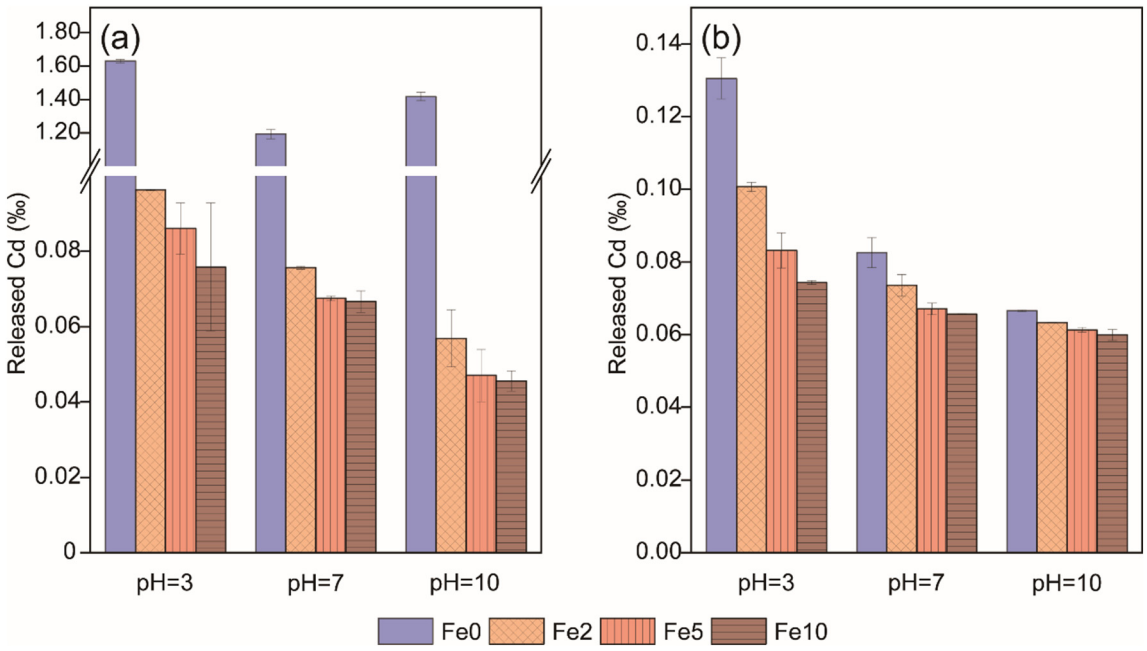


**Fig. 6.** Release of Cd during the dissolution of DCPD and its hydrolysis products (a, DCPD-5-12; b, DCPD-5-24).

(surface Cd is 10 times the bulk phase), which is inconsistent with our results. However, Zhai et al. (2018) observed nanoscale amorphous particles/clusters aggregated at the surface of DCPD with subsequent conversion to HA, agreed with our findings. Therefore, we proposed a pathway with two processes to illustrate Cd's removal mechanism by DCPD (Fig. 7c). First, Cd was immobilized on DCPD surface as weakly crystalline precipitation without affecting its mineral phase. Then, surface enriched Cd was uniformly incorporated into the HA structure as a solid-solution during its crystallization.

### 3.8. Microstructure of Fe-DCPD and enhanced Cd immobilization

During the transformation of DCPD to HA, the dissolution of DCPD plays a vital role in the transformation rate and surface reaction properties (Navarro da Rocha et al., 2018). Therefore, the change of DCPD structure by Fe incorporation could affect the dissolution properties of DCPD, which in turn affects the DCPD-HA transformation rate and the Cd removal efficiency. To verify this hypothesis, we conducted an XPS survey of Fe0 and Fe-bearing DCPD. Fig. S7 shows that Fe's substitution did not greatly change the main elemental species and groups of the outer surface layers of DCPD. The O1s peak of DCPD was dissymmetric due to the lattice oxygen (P–O; 531.25 eV) and hydroxyl group (O–H; 532.94 eV) in the DCPD (Chusuei et al., 1999). As the Fe content increased, the proportion of peaks at approximately 532.94 eV declined, indicating a reduction in interstitial water in the DCPD structure. The O—H fraction was 30.48% in Fe0, which declined to 27.21%, 27.26%, and 26.45% in Fe2, Fe5, and Fe10, respectively. These results agree with the above TG results, i.e., the interstitial water of Fe-DCPD was lower than that for Fe-free DCPD (Fig. S3b).

As discussed previously, the substitution of trivalent $Fe^{3+}$ for divalent $Ca^{2+}$ causes charge imbalance, resulting in lattice distortion and affecting the stereochemical environment of oxygen atoms linked to Ca ions. Subsequently, it caused the reduction of the interstitial water in the DCPD structure. DCPD has a layered structure held together by water molecules via hydrogen bonds (Dosen and Giese, 2011). The dehydration or hydrolysis of DCPD typically begins with breaking interlayer hydrogen bonds (Dosen and Giese, 2011; Schofield et al., 2004; Shamrai et al., 2015). The lower amount of interlayer water in Fe-DCPD indicates fewer hydrogen bonds than there were in Fe-free DCPD. Therefore, the former dehydrates or hydrolyzes more quickly than the latter. Fig. 8 clearly shows that the Fe content of DCPD was negatively related to the interlayer water and its transformation time, and positively related to the Cd removal efficiency.

### 3.9. Implication

DCPD is the initial precipitate produced after applying various phosphate fertilizers, and could also be directly used as a phosphate fertilizer (Shen et al., 2011). It can spontaneously transform into a more stable calcium phosphate mineral, such as HA (Štulajterová and Medvecký, 2008), under neutral to alkaline conditions, and this transformation process could control the migration behavior of PHEs and influence their fate (Zhai et al., 2018). Our data demonstrate that DCPD could first remove Cd as a weakly crystalline material, and will then be immobilized by the subsequently formed HA. Meanwhile, the transformation of DCPD to HA significantly reduced the risk of secondary release due to mineral dissolution. Therefore, Fe-bearing DCPD could be applied in PHEs removal/remediation as it has a superior Cd uptake capacity to Fe-free DCPD. Furthermore, Fe-bearing DCPD has a faster hydrolysis rate, allowing the transfer of Cd to HA, which is more stable, as soon as possible.

## 4. Conclusions

The structure of Fe-bearing DCPD is similar to that of Fe-free DCPD, with small lattice expansion due to the coupled substitution of $Fe^{3+}$ and $NH_4^+$ for $Ca^{2+}$. The maximum Cd uptake capacity of Fe-bearing DCPD was 431.6 mg/g, which was much higher than that of Fe-free DCPD (244.4 mg/g) and other HAP-based adsorbents. Cd was first caught by the surface of the DCPD in a weakly crystalline form and then incorporated into the structure of HA during crystallization. The dissolution experiments demonstrated that the transformation of DCPD to HA significantly reduced the risk of secondary Cd dissolution. Furthermore, the hydrolysis ability of Fe-bearing DCPD was enhanced; thus, it could transform into HA within a short time. Our results suggest that Fe-DCPD is a potential candidate for environmental remediation.

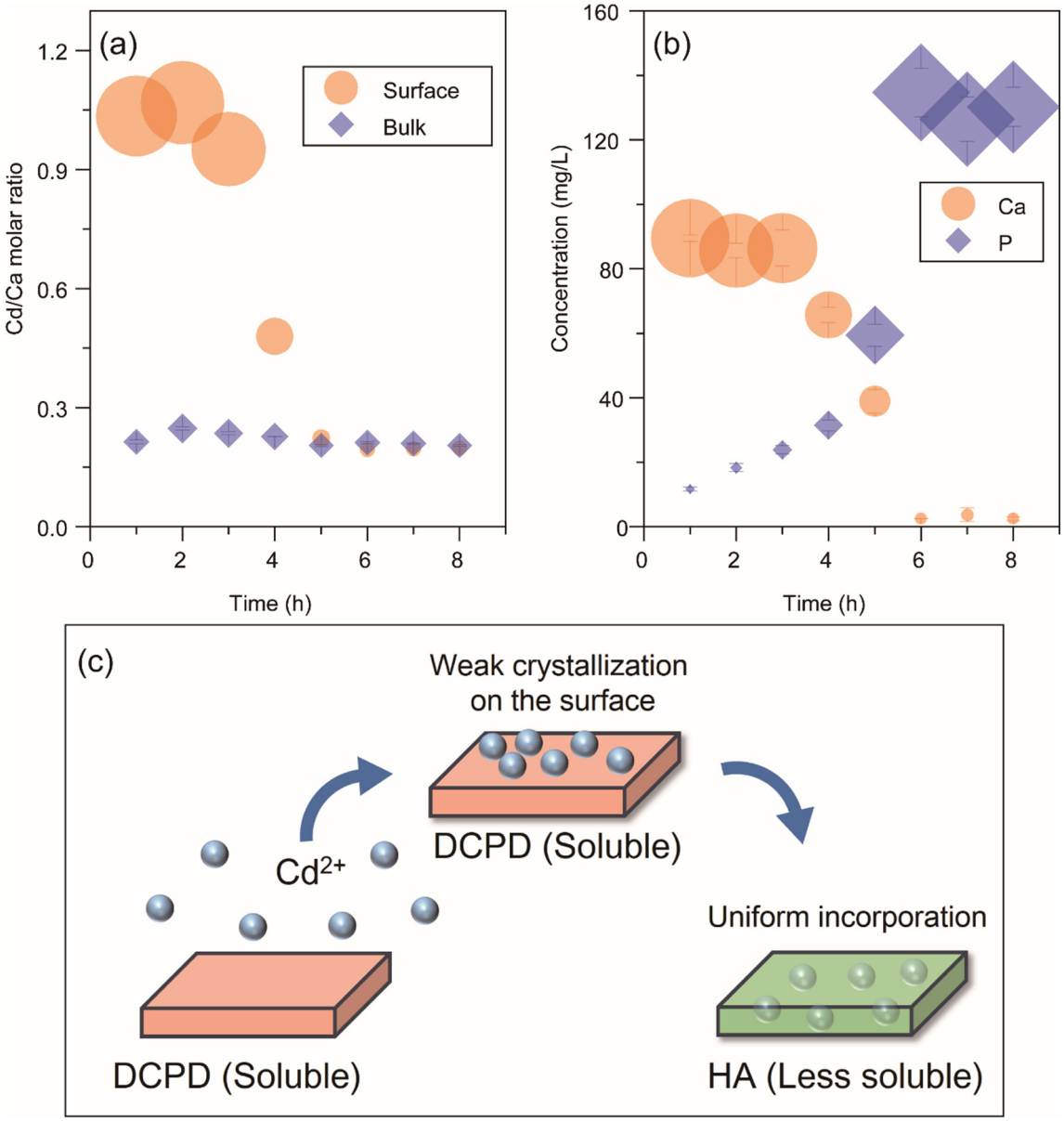


**Fig. 7.** Evolution of the Cd/Ca molar ratio of the solid phase (a) and aqueous concentrations (b) during the hydrolysis of Fe10 in the Tris-HCl solution containing 5 mM of Cd (Surface Cd/Ca molar ratio was calculated from the XPS results, and the bulk Cd/Ca molar ratio was calculated from the ICP-OES results after completely dissolving the precipitate). Schematic of the Cd removal mechanism (c).

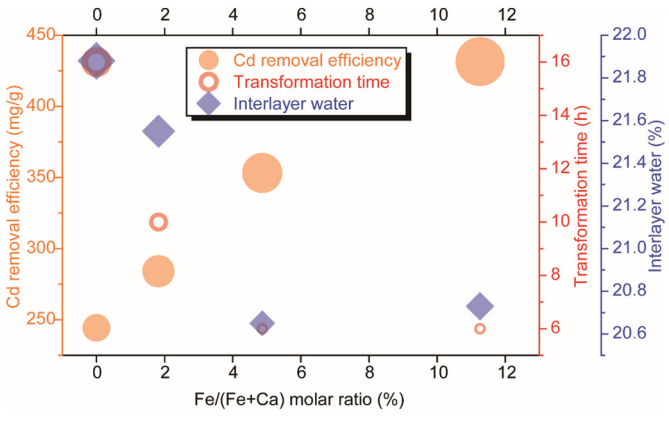


**Fig. 8.** Variations in the Cd removal efficiency, transformation time, and interlayer water with the Fe/(Fe + Ca) molar ratio.

## CRediT authorship contribution statement

**Jianan Guo:** Investigation, Visualization, Writing – original draft. **Xiaohang Zhang:** Investigation, Resources. **Maolin Wang:** Investigation, Resources. **Shijun Wu:** Conceptualization, Writing – review & editing, Supervision, Project administration, Funding acquisition. **Fanrong Chen:** Supervision, Funding acquisition. **Yongqiang Yang:** Writing – review & editing.

## Declaration of competing interest

None.

## Acknowledgments

We are grateful for the financial support provided by the National Natural Science Foundation of China (Grant No. 41877135), Science and Technology Program of Guangzhou, China (Grant No. 201804020037),

Science and Technology Planning Project of Guangdong Province (Grant Nos. 2017B020236003 and 2020B1212060055), and One-Three-Five Program of Guangzhou Institute of Geochemistry, Chinese Academy of Sciences (GIGCAS) (Grant No. 135PY201604). This is contribution No. IS-2990 from GIGCAS.

## Appendix A. Supplementary data

Evolution of the solution pH during the hydrolysis of Fe-free DCPD at different temperatures and Cd concentrations (Fig. S1); XRD pattern of DCPD after heating at varying temperatures (Fig. S2); Thermal XRD patterns, TG, and DTG curves of DCPD (Fig. S3); XRD pattern of DCPD after hydrolysis at different times (Fig. S4); SEM images of DCPD after hydrolysis (Fig. S5); SEM images of Fe0-5-2 and Fe0-5-24. TEM image and correlated TEM-EDS elemental mapping of Fe0-5-2. TEM image, HRTEM and FFT image, and EDS spectrum of Fe0-5-24.(Fig. S6); and XPS spectra for O1s, Fe2p, Ca2p, and P2p of DCPD (Fig. S7). Cd content of the samples for dissolution experiment (Table S1); Chemical composition of DCPD (Table S2); Unit cell parameters of DCPD (Table S3). Supplementary data to this article can be found online at doi: https://doi.org/10.1016/j.scitotenv.2021.146266.

## References


Alexandratos, V.G., Elzinga, E.J., Reeder, R.J., 2007. Arsenate uptake by calcite: macroscopic and spectroscopic characterization of adsorption and incorporation mechanisms. Geochim. Cosmochim. Acta 71 (17), 4172–4187. https://doi.org/10.1016/j.gca.2007.06.055.

Bamzai, K.K., Suri, S., Singh, V., 2012. Synthesis, characterization, thermal and dielectric properties of pure and cadmium doped calcium hydrogen phosphate. Mater. Chem. Phys. 135 (1), 158–167. https://doi.org/10.1016/j.matchemphys.2012.04.040.

Bao, S., Yang, W., Wang, Y., Yu, Y., Sun, Y., 2020. One-pot synthesis of magnetic graphene oxide composites as an efficient and recoverable adsorbent for Cd(II) and Pb(II) removal from aqueous solution. J. Hazard. Mater. 381, 120914. https://doi.org/10.1016/j.jhazmat.2019.120914.

Bouldin, D.R., Sample, E.C., 1959. Calcium phosphate fertilizers: IV. The relation between solubility in soils and availability coefficients of dicalcium and fused tricalcium phosphates. Soil Sci. Soc. Am. J. 23 (4), 281–285. https://doi.org/10.2136/sssaj1959.03615995002300040016x.

Camiré, C.L., Jegou Saint-Jean, S., Hansen, S., McCarthy, I., Lidgren, L., 2005. Hydration characteristics of α-tricalcium phosphates: comparison of preparation routes. J. Appl. Biomater. Biomech. 3, 106–111. https://doi.org/10.1177/228080000500300205.

Chaturvedi, S., Dave, P.N., 2012. Removal of iron for safe drinking water. Desalination. 303, 1–11. https://doi.org/10.1016/j.desal.2012.07.003.

Chien, S.H., Prochnow, L.I., Tu, S., Snyder, C.S., 2011. Agronomic and environmental aspects of phosphate fertilizers varying in source and solubility: an update review. Nutr. Cycl. Agroecosyst. 89, 229–255. https://doi.org/10.1007/s10705-010-9390-4.

Chusuei, C.C., Goodman, D.W., Van Stipdonk, M.J., Justes, D.R., Schweikert, E.A., 1999. Calcium phosphate phase identification using XPS and time-of-flight cluster SIMS. Anal. Chem. 71 (1), 149–153. https://doi.org/10.1021/ac9806963.

Colombo, C., Palumbo, G., He, J., Pinton, R., Cesco, S., 2014. Review on iron availability in soil: interaction of Fe minerals, plants, and microbes. J. Soils Sediments 14, 538–548. https://doi.org/10.1007/s11368-013-0814-z.

Conca, J.L., Wright, J., 2006. An apatite II permeable reactive barrier to remediate groundwater containing Zn. Pb and Cd. Appl. Geochemistry 21 (8), 1288–1300. https://doi.org/10.1016/j.apgeochem.2006.06.008.

Crichton, R., Crichton, R.R., Boelaert, J.R., 2001. Inorganic Biochemistry of Iron Metabolism: From Molecular Mechanisms to Clinical Consequences. 2nd ed. John Wiley & Sons, Ltd., Chichester, UK.

Cundy, A.B., Hopkinson, L., Whitby, R.L.D., 2008. Use of iron-based technologies in contaminated land and groundwater remediation: a review. Sci. Total Environ. 400 (1–3), 42–51. https://doi.org/10.1016/j.scitotenv.2008.07.002.

Dosen, A., Giese, R.F., 2011. Thermal decomposition of brushite, $CaHPO_4 \cdot 2H_2O$ to monetite $CaHPO_4$ and the formation of an amorphous phase. Am. Mineral. 96 (2–3), 368–373. https://doi.org/10.2138/am.2011.3544.

Elkady, M.F., Mahmoud, M.M., Abd-El-Rahman, H.M., 2011. Kinetic approach for cadmium sorption using microwave synthesized nano-hydroxyapatite. J. Non-Cryst. Solids 357 (3), 1118–1129. https://doi.org/10.1016/j.jnoncrysol.2010.10.021.

Fernane, F., Mecherri, M.O., Sharrock, P., Hadioui, M., Lounici, H., Fedoroff, M., 2008. Sorption of cadmium and copper ions on natural and synthetic hydroxylapatite particles. Mater. Charact. 59 (5), 554–559. https://doi.org/10.1016/j.matchar.2007.04.009.

Frey, P.A., Reed, G.H., 2012. The ubiquity of iron. ACS Chem. Biol. 7 (9), 1477–1481. https://doi.org/10.1021/cb300323q.

Fu, W., Yang, S., Yang, H., Guo, B., Huang, Z., 2019. 2D amorphous $MoS_3$ nanosheets with porous network structures for scavenging toxic metal ions from synthetic acid mine drainage. J. Mater. Chem. A 7, 18799–18806. https://doi.org/10.1039/C9TA05861C.

Gautier, M., Muller, F., Le Forestier, L., Beny, J.-M., Guegan, R., 2010. $NH_4$-smectite: characterization, hydration properties and hydro mechanical behaviour. Appl. Clay Sci. 49 (3), 247–254. https://doi.org/10.1016/j.clay.2010.05.013.

Gupta, A., Waghmare, U.V., Hegde, M.S., 2010. Correlation of oxygen storage capacity and structural distortion in transition-metal-, noble-metal-, and rare-earth-ion-substituted $CeO_2$ from first principles calculation. Chem. Mater. 22 (18), 5184–5198. https://doi.org/10.1021/cm101145d.

International Agency for Research on Cancer (IARC), 1993. Cadmium and Cadmium Compounds, Beryllium, Cadmium, Mercury, and Exposure in the Glass Manufacturing Industry, IARC Monographs on the Evaluation of Carcinogenic Risks to Humans. vol.58 pp. 121–145 (Lyon).

Järup, L., Åkesson, A., 2009. Current status of cadmium as an environmental health problem. Toxicol. Appl. Pharmacol. 238 (3), 201–208. https://doi.org/10.1016/j.taap.2009.04.020.

Kar, G., Schoenau, J., Hilger, D., Peak, D., 2017. Direct chemical speciation of soil phosphorus in a Saskatchewan Chernozem after long and short-term manure amendments. Can. J. Soil Sci. 97, 626–636. https://doi.org/10.1139/CJSS-2017-0016.

Kim, S.R., Lee, J.H., Kim, Y.T., Riu, D.H., Jung, S.J., Lee, Y.J., Chung, S.C., Kim, Y.H., 2003. Synthesis of Si, Mg substituted hydroxyapatites and their sintering behaviors. Biomaterials 24 (8), 1389–1398. https://doi.org/10.1016/S0142-9612(02)00523-9.

Knox, A.S., Kaplan, D.I., Adriano, D.C., Hinton, T.G., Wilson, M.D., 2003. Apatite and phillipsite as sequestering agents for metals and radionuclides. J. Environ. Qual. 32, 515–525. https://doi.org/10.2134/jeq2003.5150.

Kumar, M., Xie, J., Chittur, K., Riley, C., 1999. Transformation of modified brushite to hydroxyapatite in aqueous solution: effects of potassium substitution. Biomaterials 20 (15), 1389–1399. https://doi.org/10.1016/S0142-9612(99)00043-5.

Lee, D., Kumta, P.N., 2010. Chemical synthesis and stabilization of magnesium substituted brushite. Mater. Sci. Eng. C 30 (7), 934–943. https://doi.org/10.1016/j.msec.2010.04.007.

Liu, S., Li, H., Zhang, L., Feng, L., Yao, P., 2015. Strontium and magnesium substituted dicalcium phosphate dehydrate coating for carbon/carbon composites prepared by pulsed electrodeposition. Appl. Surf. Sci. 359, 288–292. https://doi.org/10.1016/j.apsusc.2015.10.134.

Madsen, H.E.L., 2008. Influence of foreign metal ions on crystal growth and morphology of brushite ($CaHPO_4$, $2H_2O$) and its transformation to octacalcium phosphate and apatite. J. Cryst. Growth 310 (10), 2602–2612. https://doi.org/10.1016/j.jcrysgro.2008.01.047.

Madsen, H.E.L., Abbona, F., Barrese, E., 2004. Effects of cadmium on crystallization of calcium phosphates. Cryst. Res. Technol. 39 (3), 235–239. https://doi.org/10.1002/crat.200310176.

Mandel, S., Tas, A.C., 2010. Brushite ($CaHPO_4 \cdot 2H_2O$) to octacalcium phosphate ($Ca_8(HPO_4)_2(PO_4)_4 \cdot 5H_2O$) transformation in DMEM solutions at 36.5 °C. Mater. Sci. Eng. C 30 (2), 245–254. https://doi.org/10.1016/j.msec.2009.10.009.

Mansour, S.F., El-dek, S.I., Ahmed, M.A., Abd-Elwahab, S.M., Ahmed, M.K., 2016. Effect of preparation conditions on the nanostructure of hydroxyapatite and brushite phases. Appl. Nanosci. 6, 991–1000. https://doi.org/10.1007/s13204-015-0509-4.

Melton, E.D., Swanner, E.D., Behrens, S., Schmidt, C., Kappler, A., 2014. The interplay of microbially mediated and abiotic reactions in the biogeochemical Fe cycle. Nat. Rev. Microbiol. 12, 797–808. https://doi.org/10.1038/nrmicro3347.

Navarro da Rocha, D., Prado da Silva, M.H., De Campos, J.B., Marçal, R.L.S.B., Mijares, D.Q., Coelho, P.G., Cruz, L.R., 2018. Kinetics of conversion of brushite coatings to hydroxyapatite in alkaline solution. J. Mater. Res. Technol. 7 (4), 479–486. https://doi.org/10.1016/j.jmrt.2018.02.002.

Pham Minh, D., Tran, N.D., Nzihou, A., Sharrock, P., 2014. Calcium phosphate based materials starting from calcium carbonate and orthophosphoric acid for the removal of lead(II) from an aqueous solution. Chem. Eng. J. 243, 280–288. https://doi.org/10.1016/j.cej.2014.01.032.

Rakovan, J., 2002. Growth and surface properties of apatite. Rev. Miner. Geochem. 48 (1), 51–86. https://doi.org/10.2138/rmg.2002.48.3.

Rubini, K., Boanini, E., Bigi, A., 2019. Role of aspartic and polyaspartic acid on the synthesis and hydrolysis of brushite. J. Funct. Biomater. 10 (1), 11. https://doi.org/10.3390/jfb10010011.

Schofield, P.F., Knight, K.S., van der Houwen, J.A.M., Valsami-Jones, E., 2004. The role of hydrogen bonding in the thermal expansion and dehydration of brushite, di-calcium phosphate dihydrate. Phys. Chem. Miner. 31, 606–624. https://doi.org/10.1007/s00269-004-0419-6.

Schumacher, M., Gelinsky, M., 2015. Strontium modified calcium phosphate cements – approaches towards targeted stimulation of bone turnover. J. Mater. Chem. B 3, 4626–4640. https://doi.org/10.1039/C5TB00654F.

Sekar, C., Kanchana, P., Nithyaselvi, R., Girija, E.K., 2009. Effect of fluorides (KF and NaF) on the growth of dicalcium phosphate dihydrate (DCPD) crystal. Mater. Chem. Phys. 115 (1), 21–27. https://doi.org/10.1016/j.matchemphys.2008.11.020.

Shamrai, V.F., Karpikhin, A.E., Fedotov, A.Y., Sirotinkin, V.P., Barinov, S.M., Komlev, V.S., 2015. Structural changes during the hydrolysis of dicalcium phosphate dihydrate to octacalcium phosphate and hydroxyapatite. Inorg. Mater. 51, 355–361. https://doi.org/10.1134/S0020168515040147.

Shannon, R.D., 1976. Revised effective ionic radii and systematic studies of interatomic distances in halides and chalcogenides. Acta Crystallogr. A 32, 751–767. https://doi.org/10.1107/S0567739476001551.

Shen, J., Yuan, L., Zhang, J., Li, H., Bai, Z., Chen, X., Zhang, W., Zhang, F., 2011. Phosphorus dynamics: from soil to plant. Plant Physiol. 156 (3), 997–1005.

Shi, H., He, F., Ye, J., 2016. Synthesis and structure of iron- and strontium-substituted octacalcium phosphate: effects of ionic charge and radius. J. Mater. Chem. B 4, 1712–1719. https://doi.org/10.1039/C5TB02247A.

Shih, W.J., Chen, Y.F., Wang, M.C., Hon, M.H., 2004. Crystal growth and morphology of the nano-sized hydroxyapatite powders synthesized from $CaHPO_4 \cdot 2H_2O$ and $CaCO_3$ by hydrolysis method. J. Cryst. Growth 270 (1–2), 211–218. https://doi.org/10.1016/j.jcrysgro.2004.06.023.

Song, Y., Yuan, P., Du, P., Deng, L., Wei, Y., Liu, D., Zhong, X., Zhou, J., 2020. A novel halloysite–$CeO_x$ nanohybrid for efficient arsenic removal. Appl. Clay Sci. 186, 105450. https://doi.org/10.1016/j.clay.2020.105450.

Štulajterová, R., Medvecký, Ľ., 2008. Effect of calcium ions on transformation brushite to hydroxyapatite in aqueous solutions. Colloids Surface. A. 316 (1–3), 104–109. https://doi.org/10.1016/j.colsurfa.2007.08.036.

Tang, X.Y., Katou, H., Suzuki, K., Ohtani, T., 2011. Air-drying and liming effects on exchangeable cadmium mobilization in contaminated soils: a repeated batch extraction study. Geoderma 161 (1–2), 18–29. https://doi.org/10.1016/j.geoderma.2010.11.012.

Tas, A.C., 2016. Transformation of brushite ($CaHPO_4 \cdot 2H_2O$) to whitlockite ($Ca_9Mg(HPO_4)(PO_4)_6$) or other CaPs in physiologically relevant solutions. J. Am. Ceram. Soc. 99 (4), 1200–1206. https://doi.org/10.1111/jace.14069.

Tas, A.C., Bhaduri, S.B., 2004. Chemical processing of $CaHPO_4 \cdot 2H_2O$: its conversion to hydroxyapatite. J. Am. Ceram. Soc. 87 (12), 2195–2200. https://doi.org/10.1111/j.1151-2916.2004.tb07490.x.

Temizel, N., Girisken, G., Tas, A.C., 2011. Accelerated transformation of brushite to octacalcium phosphate in new biomineralization media between 36.5 °C and 80 °C. Mater. Sci. Eng. C 31 (5), 1136–1143. https://doi.org/10.1016/j.msec.2011.04.009.

Ucar, S., Bjørnøy, S.H., Bassett, D.C., Strand, B.L., Sikorski, P., Andreassen, J.-P., 2017. Transformation of brushite to hydroxyapatite and effects of alginate additives. J. Cryst. Growth 468, 774–780. https://doi.org/10.1016/j.jcrysgro.2016.11.019.

Viipsi, K., Sjöberg, S., Tõnsuaadu, K., Shchukarev, A., 2013. Hydroxy- and fluorapatite as sorbents in Cd(II)–Zn(II) multi-component solutions in the absence/presence of EDTA. J. Hazard. Mater. 252–253, 91–98. https://doi.org/10.1016/j.jhazmat.2013.02.034.

Waalkes, M.P., 2000. Cadmium carcinogenesis in review. J. Inorg. Biochem. 79 (1–4), 241–244. https://doi.org/10.1016/S0162-0134(00)00009-X.

Wan, S., Wu, J., Zhou, S., Wang, R., Gao, B., He, F., 2018. Enhanced lead and cadmium removal using biochar-supported hydrated manganese oxide (HMO) nanoparticles: behavior and mechanism. Sci. Total Environ. 616–617, 1298–1306. https://doi.org/10.1016/j.scitotenv.2017.10.188.

Wang, L., Nancollas, G.H., 2008. Calcium orthophosphates: crystallization and dissolution. Chem. Rev. 108 (11), 4628–4669. https://doi.org/10.1021/cr0782574.

Wang, M., Wu, S., Guo, J., Zhang, X., Yang, Y., Chen, F., Zhu, R., 2019. Immobilization of cadmium by hydroxyapatite converted from microbial precipitated calcite. J. Hazard. Mater. 366, 684–693. https://doi.org/10.1016/j.jhazmat.2018.12.049.

World Health Organization (Ed.), 2011. Guidelines for Drinking-Water Quality, 4th ed. World Health Organization, Malta.

Xiao, J., Hu, R., Chen, G., Xing, B., 2020. Facile synthesis of multifunctional bone biochar composites decorated with Fe/Mn oxide micro-nanoparticles: physicochemical properties, heavy metals sorption behavior and mechanism. J. Hazard. Mater. 399, 123067. https://doi.org/10.1016/j.jhazmat.2020.123067.

Yukselen, M.A., Alpaslan, B., 2001. Leaching of metals from soil contaminated by mining activities. J. Hazard. Mater. 87 (1–3), 289–300. https://doi.org/10.1016/S0304-3894(01)00277-1.

Zha, R., Nadimicherla, R., Guo, X., 2014. Cadmium removal in waste water by nanostructured $TiO_2$ particles. J. Mater. Chem. A 2, 13932–13941. https://doi.org/10.1039/c4ta02106a.

Zhai, H., Wang, L., Qin, L., Zhang, W., Putnis, C.V., Putnis, A., 2018. Direct observation of simultaneous immobilization of cadmium and arsenate at the brushite–fluid interface. Environ. Sci. Technol. 52 (6), 3493–3502. https://doi.org/10.1021/acs.est.7b06479.

Zhang, J., Han, J., Wang, M., Guo, R., 2017. $Fe_3O_4$/PANI/$MnO_2$ core-shell hybrids as advanced adsorbents for heavy metal ions. J. Mater. Chem. A 5, 4058–4066. https://doi.org/10.1039/c6ta10499a.

Zhu, Z., Li, L., Zhang, H., Qiu, Y., Zhao, J., 2010. Adsorption of lead and cadmium on cadeficient hydroxyapatite. Sep. Sci. Technol. 45 (2), 262–268. https://doi.org/10.1080/01496390903423626.